

1 **Tropopause Evolution in a Rapidly Intensifying Tropical Cyclone: A Static**
2 **Stability Budget Analysis in an Idealized, Axisymmetric Framework**

3 Patrick Duran* and John Molinari

4 *University at Albany, State University of New York, Albany, NY*

5 **Corresponding author address:* Department of Atmospheric and Environmental Sciences, Univer-
6 sity at Albany, State University of New York, 1400 Washington Avenue, Albany, NY.

7 E-mail: pduran2008@gmail.com

ABSTRACT

⁸ We have some cool results!

9 **1. Introduction**

10 After undergoing a remarkably rapid intensification (RI), Hurricane Patricia (2015) set a new
11 record as the strongest tropical cyclone (TC) ever observed in the Western Hemisphere (Kim-
12 berlain et al. 2016; Rogers et al. 2017). High-altitude dropsonde observations taken during the
13 Tropical Cyclone Intensity (TCI) experiment captured this RI in unprecedented detail (Doyle et al.
14 2017). These observations revealed dramatic changes in the structure of the cold-point tropopause
15 and upper-level static stability as the storm intensified (Duran and Molinari 2018).

16 At tropical storm intensity, shortly before RI commenced, a strong inversion layer existed just
17 above Patricia’s cold-point tropopause, which was located near 17.2 km. During the first half of
18 the RI period, this inversion layer weakened throughout Patricia’s inner core, with the weakening
19 most pronounced over the developing eye. By the time the storm reached its maximum intensity,
20 the inversion layer over the eye had disappeared almost completely, which was accompanied by an
21 increase in the tropopause height to a level at or above the highest-available dropsonde data point
22 (18.3 km) at two locations. Meanwhile over the eyewall region, the static stability re-strengthened
23 and the tropopause was limited to a level at or below 17.5 km. The mechanisms that led to these
24 changes in upper-level static stability and tropopause height are the subject of the current paper.

25 Despite the importance of tropopause-layer thermodynamics in theoretical models of hurricanes
26 (Emanuel and Rotunno 2011; Emanuel 2012), few papers have examined the upper-tropospheric
27 evolution of TCs. Komaromi and Doyle (2017) found that stronger TCs tended to have a higher
28 and warmer tropopause over their inner core than weaker TCs. Their results are consistent with
29 the evolution observed over the inner core of Hurricane Patricia, in which the tropopause height
30 increased and the tropopause temperature warmed throughout RI (Duran and Molinari 2018).

31 The idealized simulations of Ohno and Satoh (2015) suggested that the development of an upper-
32 level warm core near the TC storm center acted to decrease the static stability near the tropopause.
33 Although the mechanisms that drive this static stability evolution have not been examined explic-
34 itly, Stern and Zhang (2013) described the development of the TC warm core using a potential tem-
35 perature (θ) budget analysis. They found that radial and vertical advection both played important
36 roles in warm core development throughout RI, and subgrid-scale diffusion became particularly
37 important during the later stage of RI.

38 The analysis herein is based upon that of Stern and Zhang (2013), except using a static stability
39 budget similar to that of Kepert et al. (2016) rather than a θ budget.

40 **2. Model Setup**

41 The numerical simulations were performed using version 19.4 of Cloud Model 1 (CM1) de-
42 scribed in Bryan and Rotunno (2009). The equations of motion were integrated on a 3000-km-
43 wide, 30-km-deep axisymmetric grid with 1-km horizontal and 250-m vertical grid spacing. The
44 computations were performed on an f -plane at 15°N latitude, over a sea surface with constant
45 temperature of 30.5°C, which matches that observed near Hurricane Patricia (2015; Kimberlain
46 et al. 2016). Horizontal turbulence was parameterized using the Smagorinsky scheme described in
47 Bryan and Rotunno (2009, pg. 1773), with a prescribed mixing length that varied linearly from 100
48 m at a surface pressure of 1015 hPa to 1000 m at a surface pressure of 900 hPa. This formulation
49 allows for realistically-large horizontal mixing lengths near the hurricane’s inner core, consistent
50 with the results of Bryan (2012), while not over-representing horizontal turbulence in convection
51 at outer radii. Vertical turbulence was parameterized using the formulation of Markowski and
52 Bryan (2016, their Eq. 6), using an asymptotic vertical mixing length of 100 m. A Rayleigh
53 damping layer was applied outside of the 2900-km radius and above the 25-km level to prevent

54 spurious gravity wave reflection at the model boundaries. Microphysical processes were param-
 55 eterized using the Thompson et al. (2004) microphysics scheme and radiative heating tendencies
 56 were computed every two minutes using the Rapid Radiative Transfer Model for GCMs (RRTMG)
 57 longwave and shortwave schemes (Iacono et al. 2008). The initial temperature and humidity field
 58 was horizontally homogeneous and determined by averaging all Climate Forecast System Reanal-
 59 ysis (CFSR) grid points within 100 km of Patricia’s center of circulation at 18 UTC 21 October
 60 2015. The vortex described in Rotunno and Emanuel (1987, their Eq. 37) was used to initialize
 61 the wind field, setting all parameters equal to the values used therein.

62 Although hurricanes simulated in an axisymmetric framework tend to be more intense than
 63 those observed in nature, the intensity evolution of this simulation matches reasonably well with
 64 that observed in Hurricane Patricia. After an initial spin-up period of about 20 hours, the modeled
 65 storm (Fig.1, blue lines) began an RI period that lasted approximately 30 hours. After this RI, the
 66 storm continued to intensify more slowly until the maximum 10-m wind speed reached 89 m s^{-1}
 67 and the minimum sea-level pressure reached its minimum of 846 mb, 81 hours into the simulation.
 68 Hurricane Patricia (red stars) exhibited a similar intensity evolution, with an RI period leading to a
 69 maximum 10-m wind speed of 95 m s^{-1} and a minimum sea-level pressure of 872 hPa. Despite the
 70 limitations of the axisymmetric framework, the extraordinary intensity of Hurricane Patricia and
 71 the rapidity of its intensification makes Patricia a particularly good candidate for axisymmetric
 72 analysis.

73 **3. Budget Computation**

74 The static stability can be expressed as the squared Brunt Väisälä frequency:

$$N_m^2 = \frac{g}{T} \left(\frac{\partial T}{\partial z} + \Gamma_m \right) \left(1 + \frac{T}{R_d/R_v + q_s} \frac{\partial q_s}{\partial T} \right) - \frac{g}{1 + q_t} \frac{\partial q_t}{\partial z}, \quad (1)$$

75 where g is gravitational acceleration, T is temperature, R_d and R_v are the gas constants of dry air
 76 and water vapor, respectively, q_s is the saturation mixing ratio, q_t is the total condensate mixing
 77 ratio, and Γ_m is the moist-adiabatic lapse rate:

$$\Gamma_m = g(1 + q_t) \left(\frac{1 + L_v q_s / R_d T}{c_{pm} + L_v \partial q_s / \partial T} \right), \quad (2)$$

78 where L_v is the latent heat of vaporization and c_{pm} is the specific heat of moist air at constant
 79 pressure. In the tropopause layer, q_s , $\partial q_s / \partial T$, and $\partial q_t / \partial z$ approach zero. In this limiting case,
 80 Eq. 1 reduces to:

$$N^2 = \frac{g}{\theta} \frac{\partial \theta}{\partial z}, \quad (3)$$

81 where θ is the potential temperature.

82 To compute N^2 , CM1 uses Eq.1 in saturated environments and Eq. 3 in sub-saturated environ-
 83 ments. For simplicity, however, only Eq. 3 will be employed for the budget computations herein¹.

84 Taking the time derivative of Eq. 3 yields the static stability tendency:

$$\frac{\partial N^2}{\partial t} = \frac{g}{\theta} \frac{\partial}{\partial z} \frac{\partial \theta}{\partial t} - \frac{g}{\theta^2} \frac{\partial \theta}{\partial z} \frac{\partial \theta}{\partial t}, \quad (4)$$

85 where the potential temperature tendency, $\partial \theta / \partial t$, can be written:

$$\frac{\partial \theta}{\partial t} = HADV + VADV + HTURB + VTURB + MP + RAD + DISS \quad (5)$$

86 Each term on the right-hand side of Eq. 5 represents a θ budget variable, each of which is out-
 87 put directly by the model every minute. HADV and VADV are the radial and vertical advective
 88 tendencies², HTURB and VTURB are the radial and vertical tendencies from the turbulence pa-
 89 rameterization, MP is the tendency from the microphysics scheme, RAD is the tendency from the
 90 radiation scheme, and DISS is the tendency due to turbulent dissipation. This equation neglects
 91 Rayleigh damping, since this term is zero everywhere below 25 km, and the analysis domain does

¹The validity of this approximation will be substantiated later in this section.

²These terms include the tendencies due to diffusion that are implicit in the fifth-order advection scheme.

not extend to that level. Each term in Eq. 5 is substituted for $\partial\theta/\partial t$ in Eq. 4, yielding the contribution of each budget term to the static stability tendency. These terms are summed, yielding an instantaneous "budget change" in N^2 every minute. The budget changes are then averaged over 24-hour periods and compared to the total model change in N^2 over that same time period, i.e.:

$$\Delta N_{budget}^2 = \frac{1}{\delta t} \sum_{t=t_0}^{t_0+\delta t} \frac{\partial N^2}{\partial t} \bigg|_t \quad (6)$$

$$\Delta N_{model}^2 = N_{t_0+\delta t}^2 - N_{t_0}^2 \quad (7)$$

$$Residual = \Delta N_{model}^2 - \Delta N_{budget}^2 \quad (8)$$

where t_0 is an initial time and δt is 24 hours.

Eqs. 6-8 are plotted for four consecutive 24-hour periods in Fig. 2. For this and all subsequent radial-vertical cross sections, a 1-2-1 smoother is applied once in the radial direction to eliminate $2\Delta r$ noise that appears in some of the raw model output and calculated fields. The left column of Fig. 2 depicts the model changes (Eq. 7), the center column depicts the budget changes (Eq. 6), and the right column depicts the residuals (Eq. 8). In every 24-hour period, the budget changes are nearly identical to the model changes, which is reflected in the near-zero residuals in the right column. This indicates that the budget accurately represents the model variability, which implies that the neglect of moisture in the budget computation introduces negligible error within the analysis domain³.

In the tropopause layer, some of the budget terms are small enough to be ignored. To determine which of the budget terms are most important, a time series of the contribution of each of the budget terms in Eq. 5 to the tropopause-layer static stability tendency is plotted in Fig. 4. For this figure, each of the budget terms is computed using the method described in Section 3, except with

³This is not the case in the lower- and mid-troposphere, where the residual actually exceeds the budget variability in many places, likely due to the neglect of moisture; thus we limit this analysis to the upper troposphere and lower stratosphere.

112 1-hour averaging intervals instead of 24-hour intervals. The absolute values of these tendencies
113 are then averaged over a radius-height domain surrounding the tropopause and plotted as a time
114 series⁴. Advection (Fig. 4, red line) plays an important role in the mean tropopause-layer static
115 stability tendency at all times, and vertical turbulence (Fig. 4, blue line) and radiation (Fig. 4, dark
116 green line) also contribute significantly. Although the contribution from horizontal turbulence
117 (Fig. 4, purple line) becomes more important after 48 hours, it is confined to a very small region
118 immediately surrounding the eyewall tangential velocity maximum (not shown), and is negligible
119 throughout the rest of the tropopause layer. The remaining two processes - microphysics and
120 dissipative heating (Fig. 4, orange and light green lines, respectively) - lie atop one another near
121 zero. These time series indicate that, at all times, three budget terms dominate the tropopause-layer
122 static stability tendency: advection, vertical turbulence, and radiation. Variations in the magnitude
123 and spatial structure of these terms drive the static stability changes depicted in Fig. 2; subsequent
124 sections will focus on these variations and what causes them.

125 4. Results

126 a. Static stability evolution

127 The average N^2 over the first day of the simulation (Fig. 3a) indicates the presence of a weak
128 static stability maximum just above the cold-point tropopause. Over the subsequent 24 hours,
129 during the RI period, the static stability within and above this layer decreased near the storm
130 center (Fig. 3b). This decreasing N^2 corresponded to an increase in the tropopause height within
131 the developing eye, maximized at the storm center. Outside of the eye, meanwhile, the tropopause

⁴It will be seen in subsequent figures that each of the terms contributes both positively and negatively to the N^2 tendency within the analysis domain. Thus, taking an average over the domain tends to wash out the positive and negative contributions. To circumvent this problem, the absolute value of each of the terms is averaged.

height decreased over the eyewall region (25-60-km radius) and increased only slightly outside of the 60-km radius. In this outer region, the N^2 maximum just above the tropopause strengthened during RI. These trends continued as the storm's intensity leveled off in the 48-72-hour period (Fig. 3c). The tropopause height increased to nearly 21 km at the storm center and sloped sharply downward to 16.3 km on the inner edge of the eyewall, near the 30 km radius. Static stability outside of the eye, meanwhile, continued to increase just above the cold-point tropopause. This N^2 evolution closely follows that observed in Hurricane Patricia (2015; Duran and Molinari 2018). The mechanisms that led to these static stability changes will be investigated in the subsequent sections.

b. Static stability budget analysis

(i) 0-24 hours The weakening of the lower-stratospheric static stability maximum during the initial spin-up period is reflected in the total N^2 budget change over this time (Fig. 5a). The 17-18-km layer was characterized by decreasing N^2 (purple shading), maximizing at the storm center. The layer immediately below the tropopause, meanwhile, saw strengthening N^2 during this time period. Although these tendencies extended out to the 200-km radius, they were particularly pronounced at innermost radii. A comparison of the contributions of advection (Fig. 5b), vertical turbulence (Fig. 5c), and radiation (Fig. 5d) reveals that advection is primarily responsible for the change in static stability during this period. Although vertical turbulence acts in opposition to advection (i.e. it acts to stabilize regions that advection acts to destabilize), the magnitude of the advective tendencies is larger, particularly at the innermost radii. The sum of advection and vertical turbulence (Fig. 5e) almost exactly replicates the static stability tendencies above 17 km. Radiative tendencies (Fig. 5d) act to destabilize the layer below about 16 km and stabilize the

154 layer between 16 and 17 km. The sum of advection, vertical turbulence, and radiation (Fig. 5f)
155 reproduces the total change in N^2 almost exactly.

156 ...Explain this in the context of radial and vertical velocities... ...See Stern and Zhang, Page 84,
157 Section 3d... ...Add mention of total condensate and radiative heating tendencies as it relates to
158 stability tendency due to rad...

159 (ii) *24-48 hours* During the RI period, N^2 within the eye generally decreased above 16 km and
160 increased below (Fig. 6a). These tendencies at the innermost radii were driven almost entirely by
161 advection (Fig. 6b); vertical turbulence (Fig. 6c) and radiation (Fig. 6d) contributed negligibly to
162 the static stability tendencies in this region.

163 Outside of the eye, the N^2 evolution exhibited alternating layers of positive and negative tenden-
164 cies. Near and above 18 km existed an upward-sloping region of decreasing N^2 that extended out
165 to the 180-km radius. In this region, neither vertical turbulence nor radiation exhibited negative
166 N^2 tendencies; advection was the only forcing for destabilization. Immediately below this layer
167 was a region of increasing N^2 , which sloped upward from 17 km near the 30-km radius to just
168 below 18 km outside of the 100-km radius. Advection and vertical turbulence both contributed to
169 this positive N^2 tendency, with advection playing an important role below about 17.5 km and and
170 turbulence playing an important role above. The sum of advection and turbulence (Fig. 6e) reveals
171 two discontinuous regions of increasing N^2 in the 17-18-km layer rather than one contiguous re-
172 gion. The addition of radiation to these two terms, however, (Fig. 6f) provides the link between
173 these two regions, indicating that radiation also plays a role in strengthening the stable layer just
174 above the tropopause. In the 16-17-km layer, a horizontally-extensive layer of decreasing N^2 also
175 was forced by a combination of advection, vertical turbulence, and radiation. The sum of advec-
176 tion and vertical turbulence accounts for only a portion of the decreasing N^2 in this layer, and

177 actually indicates forcing for stabilization near the 50-km radius and outside of the 130-km radius.
178 Radiative tendencies overcome this forcing for stabilization in both of these regions to produce the
179 radially-extensive region of destabilization observed just below the tropopause.

180 TWO REGIONS WHERE Panel (f) differs from panel (a): 30-60 km radial band below 16 km,
181 which is actually canceled out by a vertical gradient of latent heating, and the thin region of strong
182 stabilization between 15-17.5 km near $r=30$ km, which is canceled out by horizontal turbulence.

183 (iii) 48-72 hours After the storm's maximum wind speed leveled off near 80 m s^{-1} , the magnitude
184 of the static stability tendencies within the eye decreased to near zero (Fig. 7a).

185 Outside of the eye, however, N^2 continued to increase just above the tropopause and decrease
186 just below. The sum of advection and vertical turbulence (Fig. 7e) indicates that the increase
187 of N^2 observed in the 17-18-km layer and inside of the 80-km radius cannot be attributed to
188 these processes, since the sum of these two terms provided forcing for destabilization. Instead,
189 radiation (Fig. 7d), provided the forcing for stabilization in this region. Outside of the 80-km
190 radius, both advection (Fig. 7b) and vertical turbulence (Fig. 7c) provided forcing for stabilization
191 near the 18-km level. The sum of the two terms indicates increasing N^2 near the 18-km level
192 everywhere outside of the 80-km radius, but this stabilization is slightly weaker in the 90-120-km
193 radial band than the observed value. The addition of radiation (Fig. 7f) provides the extra forcing
194 for stabilization required to account for the observed increase in N^2 . Outside of the 120-km radius,
195 the region of radiative forcing for stabilization slopes downward, and the increase in N^2 observed
196 near 18 km can be explained entirely by a combination of advection and vertical turbulence. The
197 layer of decreasing N^2 observed near 17 km was forced primarily by vertical turbulence and
198 radiation. Within most of this region, advection provided strong forcing for stabilization, but

199 this forcing was outweighed by the negative N^2 tendencies induced by a combination of vertical
 200 turbulence and radiation.

201 5. Discussion

202 a. The role of advection

203 Advection played an important role in the tropopause-layer N^2 evolution at all stages of intensi-
 204 fication, but for brevity, this section will focus only on the RI period. To investigate the advective
 205 processes more closely, the individual contributions of horizontal and vertical advection during
 206 the RI period are shown in Fig. 8, along with the corresponding time-mean radial and vertical ve-
 207 locities and θ . The N^2 tendencies due to the two advective components (Fig. 8a,b) exhibit strong
 208 cancellation, consistent with flow that is nearly isentropic. There are, however, some regions in
 209 which flow crosses θ surfaces; this flow accounts for all non-zero N^2 tendencies due to advection
 210 previously seen in Fig. 6b.

211 Some insight can be gained by considering the time tendency of the vertical θ gradient due to
 212 advection:

$$\left(\frac{\partial}{\partial t} \frac{\partial \theta}{\partial z} \right)_{adv} = -u \frac{\partial}{\partial r} \frac{\partial \theta}{\partial z} - w \frac{\partial}{\partial z} \frac{\partial \theta}{\partial z} - \frac{\partial u}{\partial z} \frac{\partial \theta}{\partial r} - \frac{\partial w}{\partial z} \frac{\partial \theta}{\partial z}. \quad (9)$$

213 The first two terms on the right-hand side of Eq. 9 represent advection of static stability by the
 214 radial and vertical wind, respectively. The third and fourth terms represent, respectively, the tilting
 215 of isentropes in the presence of vertical wind shear, and the spreading or compaction of isentropes
 216 through divergence of the vertical wind.

217 During the RI period, strong radial and vertical circulations developed near the tropopause,
 218 which forced high-magnitude N^2 tendencies due to advection (Fig. 8a,b). A layer of strong outflow
 219 developed at and below the tropopause during this period, with the outflow maximum (dashed cyan

220 line) curving from the 14-km level at the 50-km radius to just below the 16-km level outside of
 221 the 80-km radius (Fig. 8c). The cyan line, by definition, represents the level at which the vertical
 222 gradient of radial velocity switched signs, with $\partial u / \partial z > 0$ below the line and $\partial u / \partial z < 0$ above.
 223 Notably, the N^2 tendency due to horizontal advection (Fig. 8a) also tended to switch signs very
 224 near this line, with stabilization below the outflow maximum and destabilization above. This
 225 suggests that vertical wind shear above and below the outflow maximum played an important
 226 role in the N^2 tendency during this time. Examination of the third term on the right-hand side
 227 of Eq. 9 reveals that tilting of isentropes within these shear layers contributed to the strong N^2
 228 tendencies that flanked the outflow maximum. Outside of the eye and eyewall, isentropes generally
 229 sloped upward with radius, which means that θ decreased outward ($\partial \theta / \partial r < 0$). Thus, wherever
 230 $\partial u / \partial z > 0$, the tilting term forced an increase in N^2 , and wherever $\partial u / \partial z < 0$, the tilting term
 231 forced a decrease in N^2 . This is precisely the structure seen in Fig. 8a, which suggests that the
 232 tilting term

233 Meanwhile in the lower stratosphere, a thin layer of 2-4 m s⁻¹ inflow developed a few hundred
 234 meters above the tropopause.

235 Radiative heating and turbulence viscosity figures?

236 Discuss how turbulence increases the static stability in some regions – vertical gradients of
 237 turbulence intensity.

238 Diurnal variability of static stability in the upper troposphere is an interesting area of future
 239 research.

240 *Acknowledgments.* We are indebted to George Bryan for his continued development and support
 241 of Cloud Model 1. We also thank Jeffrey Kepert, Robert Fovell, and Erika Navarro for helpful
 242 conversations related to this work. ADD GRANT NUMBER

APPENDIX

Sensitivity experiments

The simulations exhibited some sensitivity to the initial thermodynamic profile and the prescribed vertical mixing length. Although the details of the intensification and the tropopause-layer N^2 evolution varied when these quantities were changed, the conclusions of the paper remain unchanged.

a. Sensitivity to the initial thermodynamic profile

A number of sensitivity experiments were conducted using a variety of initial soundings. Changing the initial temperature and humidity profiles affected the timing of the onset of organized deep convection and the rapidity of intensification. In all simulations, however, convection eventually penetrated to the tropopause, at which time vertical turbulence and radiation combined with advection to adjust the N^2 profile toward that which was observed in the control run. By the end of the RI period in every simulation, all three processes were actively modifying the N^2 profile near the tropopause.

b. Sensitivity to the vertical mixing length

The extent of parameterized turbulent mixing is highly dependent on a prescribed length scale. Since there is no theoretical or observational guidance for the selection of this mixing length, the value used in the control run (100 m) is based on the sensitivity experiments of BRYAN 2012???? Since the vertical eddy viscosity varies linearly with the vertical mixing length, prescribing a smaller mixing length produces smaller θ tendencies due to turbulence. Even with a mixing length on the low end of those tested by BRYAN 2012????, however, turbulence still plays a role in the tropopause-layer N^2 evolution. FIG shows the N^2 evolution in a simulation identical to the

control run, except with a vertical mixing length of 50 m rather than 100 m. DESCRIPTION OF
THE FIGURE

References

Bryan, G. H., 2012: Effects of surface exchange coefficients and turbulence length scales on the
intensity and structure of numerically simulated hurricanes. *Mon. Wea. Rev.*, **140**, 1125–1143.

Bryan, G. H., and R. Rotunno, 2009: The maximum intensity of tropical cyclones in axisymmetric
numerical model simulations. *Mon. Wea. Rev.*, **137**, 1770–1789.

Doyle, J. D., and Coauthors, 2017: A view of tropical cyclones from above: The Tropical Cyclone
Intensity (TCI) Experiment. *Bull. Amer. Meteor. Soc.*, **98**, 2113–2134.

Duran, P., and J. Molinari, 2018: Dramatic inner-core tropopause variability during the rapid
intensification of Hurricane Patricia (2015). *Mon. Wea. Rev.*, **XXX**, XXX–XXX.

Emanuel, K., 2012: Self-stratification of tropical cyclone outflow. Part II: Implications for storm
intensification. *J. Atmos. Sci.*, **69**, 988–996.

Emanuel, K., and R. Rotunno, 2011: Self-stratification of tropical cyclone outflow. Part I: Impli-
cations for storm structure. *J. Atmos. Sci.*, **68**, 2236–2249.

Iacono, M. J., J. S. Delamere, E. J. Mlawer, M. W. Shephard, S. A. Clough, and W. D. Collins,
2008: Radiative forcing by long-lived greenhouse gases: Calculations with the AER radiative
transfer models. *J. Geophys. Res.*, **113** (D13103).

Kepert, J. D., J. Schwendike, and H. Ramsay, 2016: Why is the tropical cyclone boundary layer
not “well mixed”? *J. Atmos. Sci.*, **73**, 957–973.

284 Kimberlain, T. B., E. S. Blake, and J. P. Cangialosi, 2016: Tropical cyclone report: Hurricane
 285 Patricia. National Hurricane Center. [Available online at www.nhc.noaa.gov].

286 Komaromi, W. A., and J. D. Doyle, 2017: Tropical cyclone outflow and warm core structure as
 287 revealed by HS3 dropsonde data. *Mon. Wea. Rev.*, **145**, 1339–1359.

288 Markowski, P. M., and G. H. Bryan, 2016: LES of laminar flow in the PBL: A potential problem
 289 for convective storm simulations. *Mon. Wea. Rev.*, **144**, 1841–1850.

290 Ohno, T., and M. Satoh, 2015: On the warm core of a tropical cyclone formed near the tropopause.
 291 *J. Atmos. Sci.*, **72**, 551–571.

292 Rogers, R. F., S. Aberson, M. M. Bell, D. J. Cecil, J. D. Doyle, J. Morgerman, L. K. Shay, and
 293 C. Velden, 2017: Re-writing the tropical record books: The extraordinary intensification of
 294 Hurricane Patricia (2015). *Bull. Amer. Meteor. Soc.*, **98**, 2091–2112.

295 Rotunno, R., and K. A. Emanuel, 1987: An air-sea interaction theory for tropical cyclones. Part II:
 296 Evolutionary study using a nonhydrostatic axisymmetric numerical model. *J. Atmos. Sci.*, **44**,
 297 542–561.

298 Stern, D. P., and F. Zhang, 2013: How does the eye warm? Part I: A potential temperature budget
 299 analysis of an idealized tropical cyclone. *J. Atmos. Sci.*, **70**, 73–89.

300 Thompson, G., R. M. Rasmussen, and K. Manning, 2004: Explicit forecasts of winter precipitation
 301 using an improved bulk microphysics scheme. Part I: Description and sensitivity analysis. *Mon.*
 302 *Wea. Rev.*, **132**, 519–542.

LIST OF FIGURES

| | | |
|-----------------|--|----|
| Fig. 1. | The maximum 10-m wind speed (top panel; m s^{-1}) and minimum sea-level pressure (bottom panel; hPa) in the simulated storm (blue lines) and from Hurricane Patricia's best track (red stars). | 18 |
| Fig. 2. | Left panels: Twenty-four-hour changes in squared Brunt-Väisälä frequency (N^2 ; 10^{-4} s^{-2}) over (a) 0-24 hours, (b) 24-48 hours, (c) 48-72 hours. Middle Panels: The N^2 change over the same time periods computed using Eqs. 4-6, Right Panels: The budget residual over the same time periods, computed by subtracting the budget change (middle column) from the model change (left column). | 19 |
| Fig. 3. | Twenty-four-hour averages of squared Brunt-Väisälä frequency (N^2 ; 10^{-4} s^{-2}) over (a) 0-24 hours, (b) 24-48 hours, (c) 48-72 hours. Orange lines represent the cold-point tropopause averaged over the same time periods. | 20 |
| Fig. 4. | Time series of the contribution of each of the budget terms to the time tendency of the squared Brunt-Väisälä frequency (N^2 ; 10^{-4} s^{-2}). For each budget term, the absolute value of the N^2 tendency is averaged temporally over 1-hour periods (using output every minute), and spatially in a region extending from 0 to 200 km radius and 14 to 21 km altitude. | 21 |
| Fig. 5. | (a) Total change in N^2 over the 0-24-hour period ($10^{-4} \text{ s}^{-2} (24 \text{ hr})^{-1}$) and the contributions to that change from (b) the sum of horizontal and vertical advection, (c) vertical turbulence, (d) longwave and shortwave radiation, (e) the sum of horizontal advection, vertical advection, and vertical turbulence, and (f) the sum of horizontal advection, vertical advection, vertical turbulence, and longwave and shortwave radiation. | 22 |
| Fig. 6. | As in Fig. 5, but for the 24-48-hour period. | 23 |
| Fig. 7. | As in Fig. 5, but for the 48-72-hour period. | 24 |
| Fig. 8. | The contribution to the change in N^2 over the 24-48-hour period ($10^{-4} \text{ s}^{-2} (24 \text{ hr})^{-1}$) by (a) horizontal advection and (b) vertical advection. (c) The radial velocity (m s^{-1} ; filled contours), potential temperature (K; thick black contours), cold-point tropopause height (orange line), and level of maximum outflow (dashed cyan line) averaged over the 24-48-hour period. (d) The vertical velocity (cm s^{-1} ; filled contours), potential temperature (K; thick black contours), and cold-point tropopause height (orange line) averaged over the 24-48-hour period. | 25 |
| Fig. 9. | Ice mixing ratio (g kg^{-1}) and cold-point tropopause height (orange lines) averaged over (a) 0-24 hours, (c) 24-48 hours, and (e) 48-72 hours. Radiative heating rate (K hr^{-1}) and cold-point tropopause height (orange lines) averaged over (b) 0-24 hours, (d) 24-48 hours, and (f) 48-72 hours. | 26 |
| Fig. 10. | Vertical eddy diffusivity ($\text{m}^2 \text{ s}^{-2}$; filled contours), cold-point tropopause height (cyan lines), and radial velocity (m s^{-1} ; thick black lines) averaged over (a) 0-24 hours, (b) 24-48 hours, and (c) 48-72 hours. | 27 |

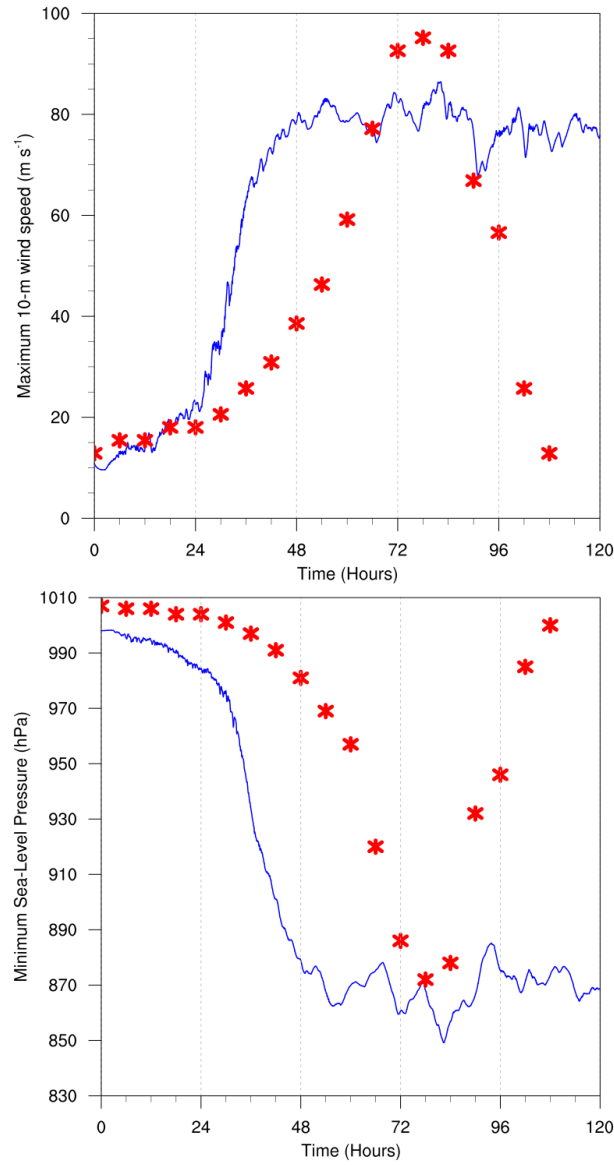
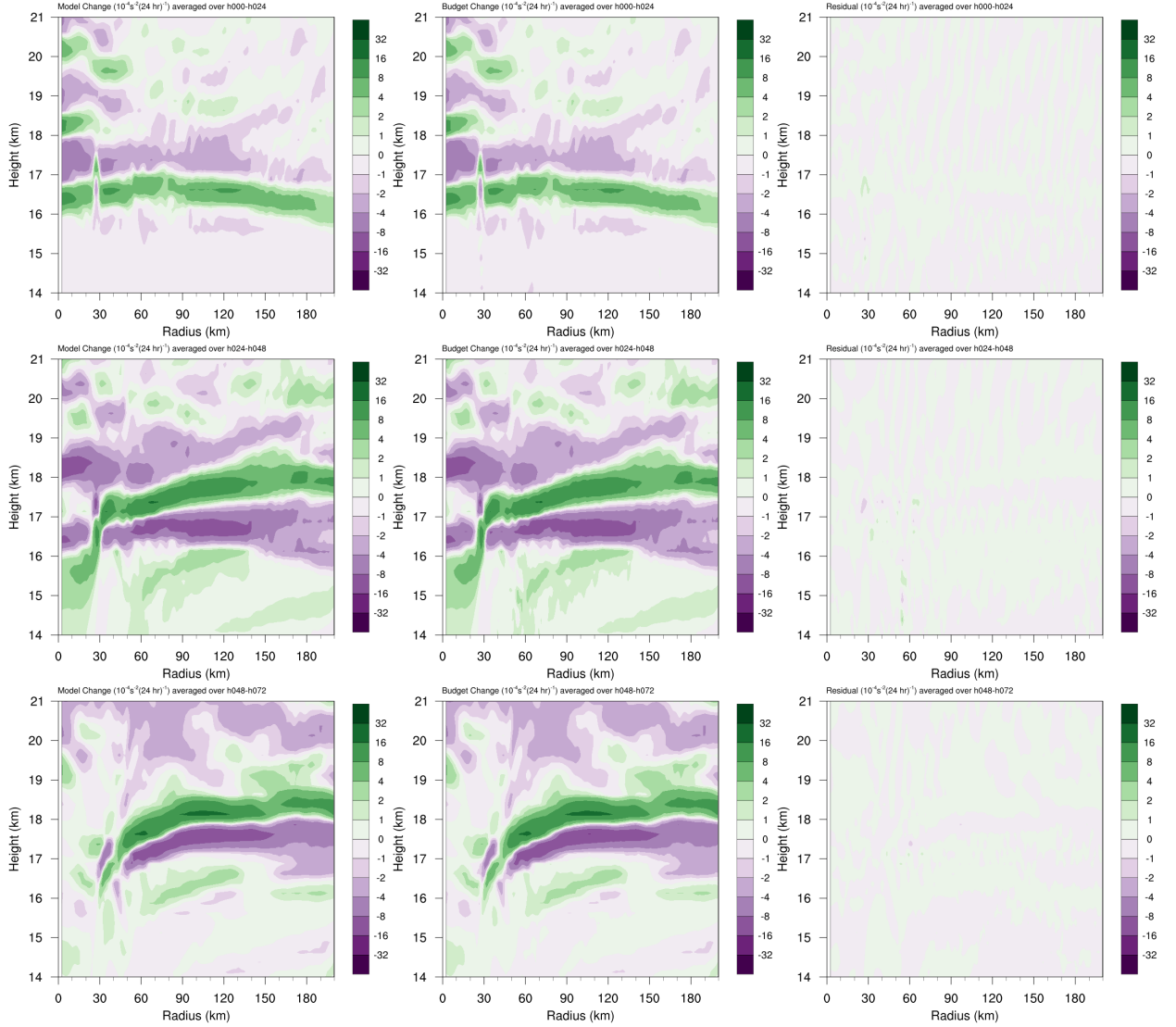


FIG. 1. The maximum 10-m wind speed (top panel; m s^{-1}) and minimum sea-level pressure (bottom panel; hPa) in the simulated storm (blue lines) and from Hurricane Patricia's best track (red stars).



342 FIG. 2. Left panels: Twenty-four-hour changes in squared Brunt-Väisälä frequency (N^2 ; 10^{-4} s^{-2}) over (a) 0-
 343 24 hours, (b) 24-48 hours, (c) 48-72 hours. Middle Panels: The N^2 change over the same time periods computed
 344 using Eqs. 4-6, Right Panels: The budget residual over the same time periods, computed by subtracting the
 345 budget change (middle column) from the model change (left column).

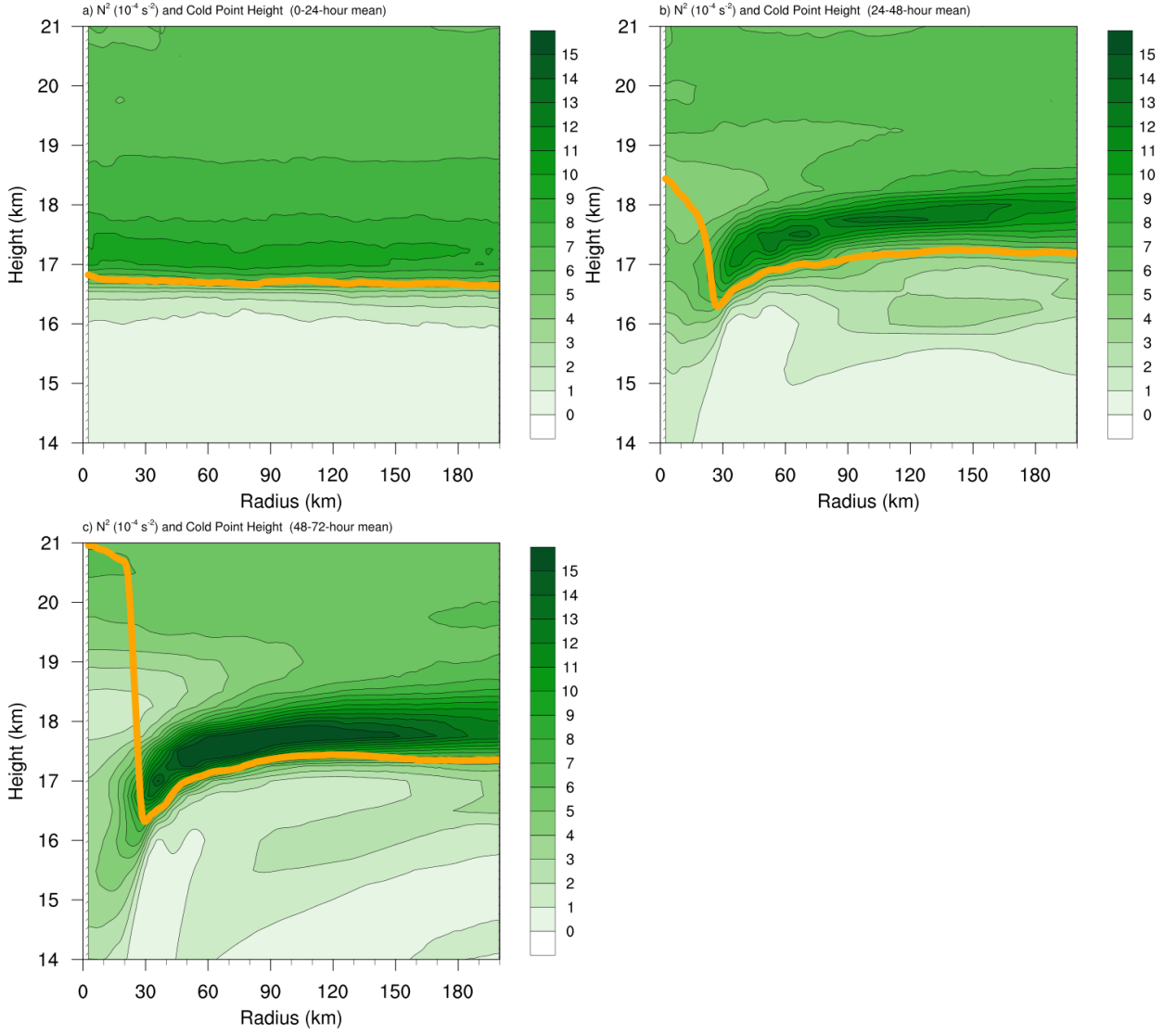


FIG. 3. Twenty-four-hour averages of squared Brunt-Väisälä frequency (N^2 ; 10^{-4} s^{-2}) over (a) 0-24 hours, (b) 24-48 hours, (c) 48-72 hours. Orange lines represent the cold-point tropopause averaged over the same time periods.

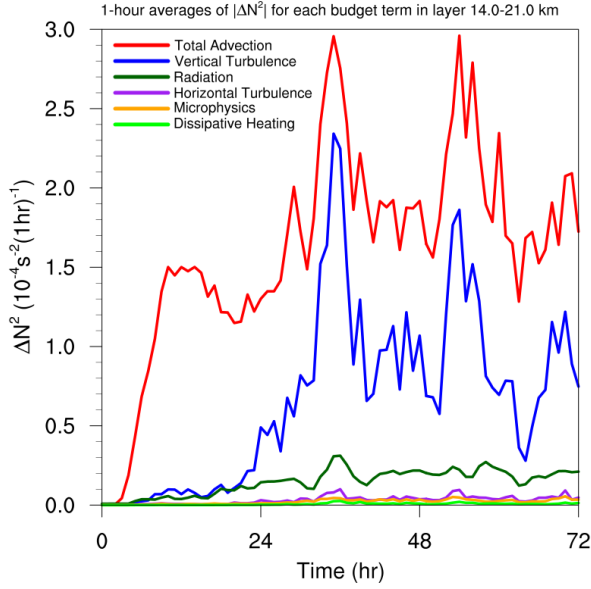
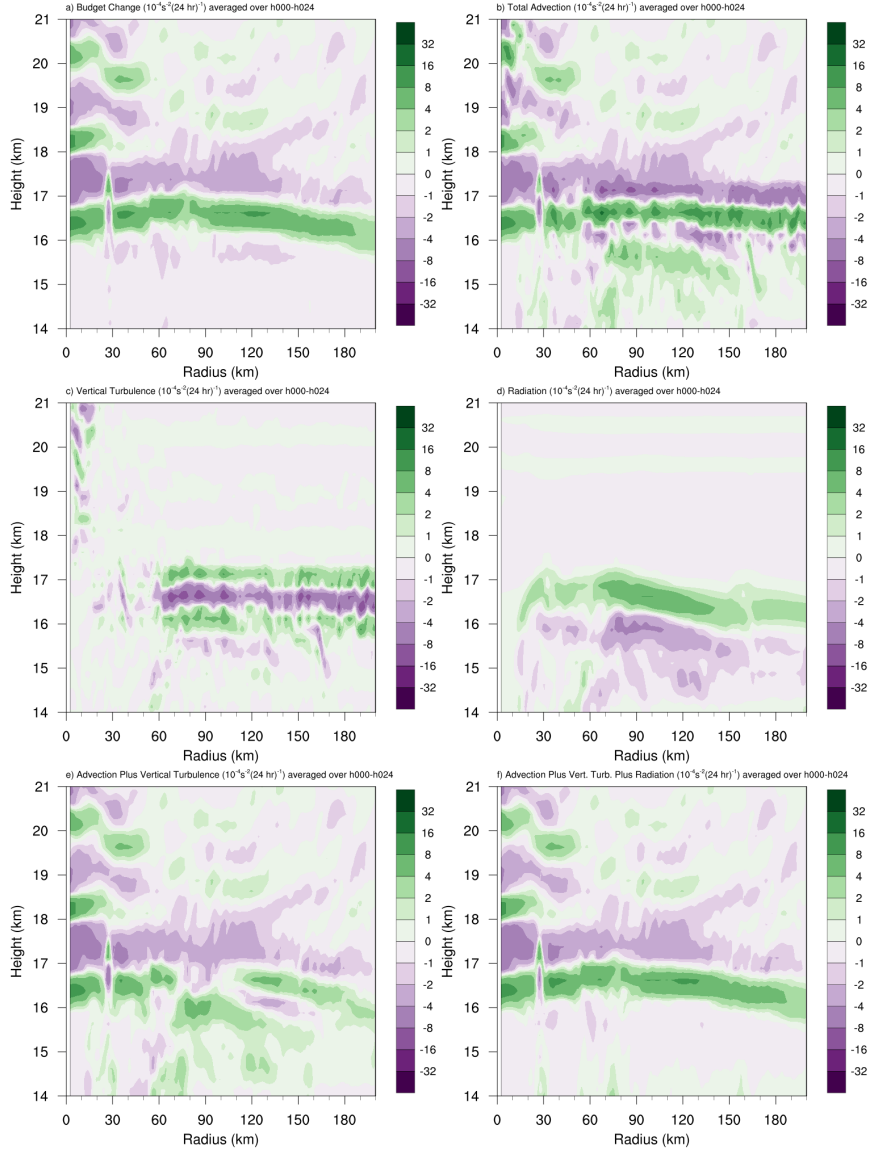


FIG. 4. Time series of the contribution of each of the budget terms to the time tendency of the squared Brunt-Väisälä frequency (N^2 ; 10^{-4} s^{-2}). For each budget term, the absolute value of the N^2 tendency is averaged temporally over 1-hour periods (using output every minute), and spatially in a region extending from 0 to 200 km radius and 14 to 21 km altitude.



353 FIG. 5. (a) Total change in N^2 over the 0-24-hour period ($10^{-4} \text{ s}^{-2} (24 \text{ hr})^{-1}$) and the contributions to that
 354 change from (b) the sum of horizontal and vertical advection, (c) vertical turbulence, (d) longwave and shortwave
 355 radiation, (e) the sum of horizontal advection, vertical advection, and vertical turbulence, and (f) the sum of
 356 horizontal advection, vertical advection, vertical turbulence, and longwave and shortwave radiation.

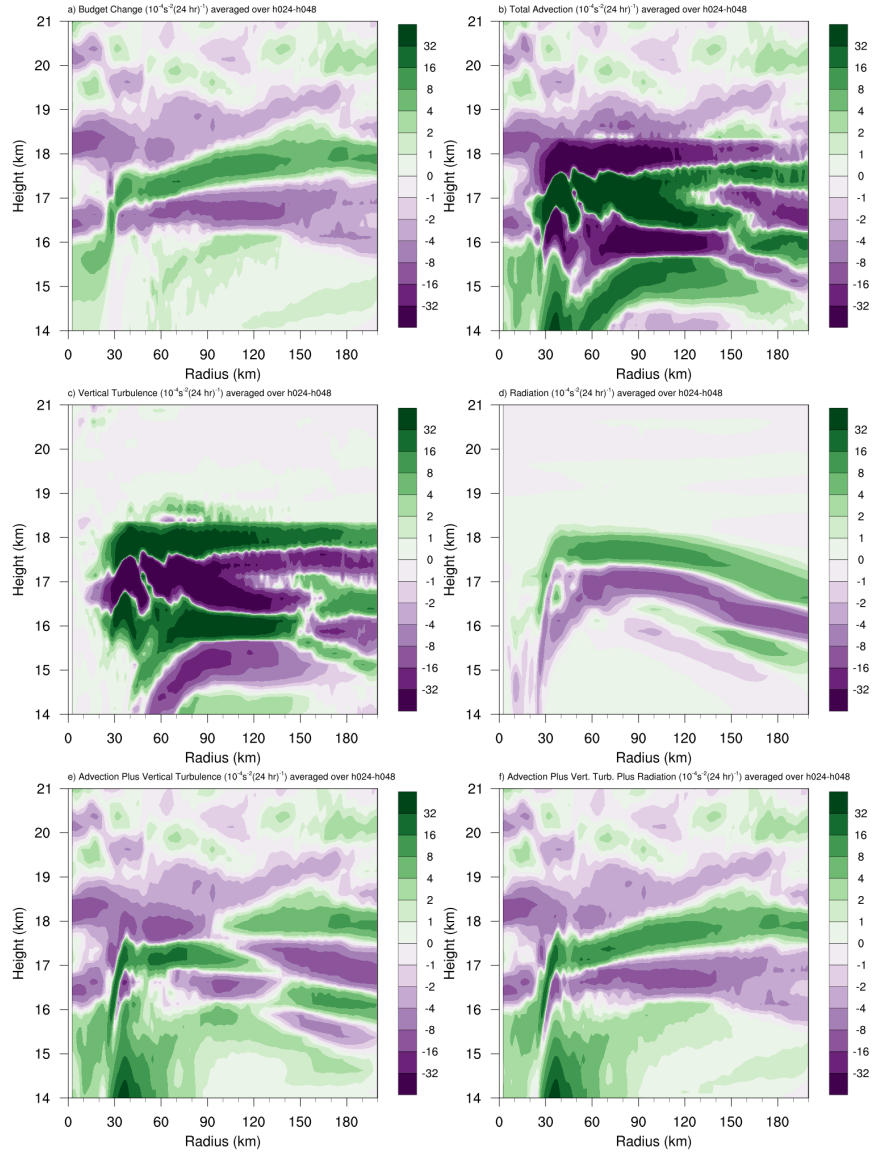


FIG. 6. As in Fig. 5, but for the 24-48-hour period.

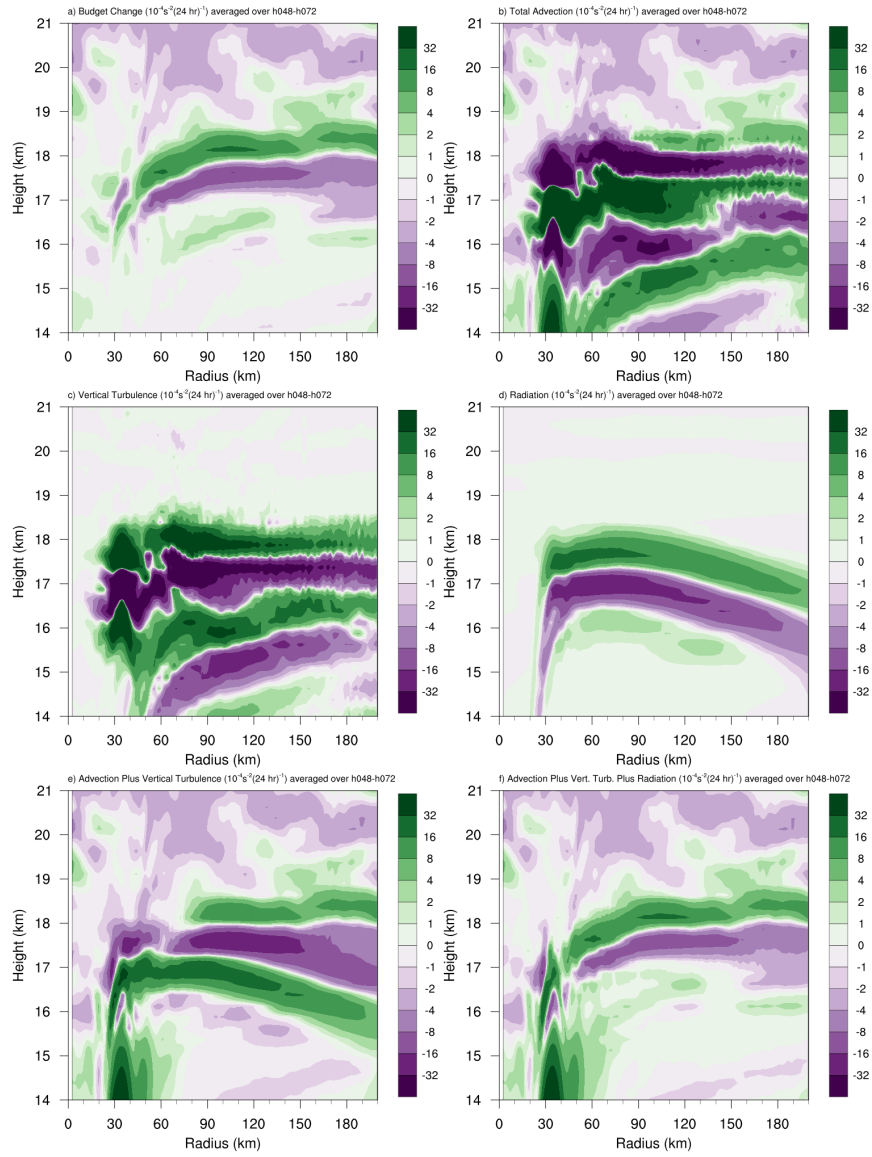


FIG. 7. As in Fig. 5, but for the 48-72-hour period.

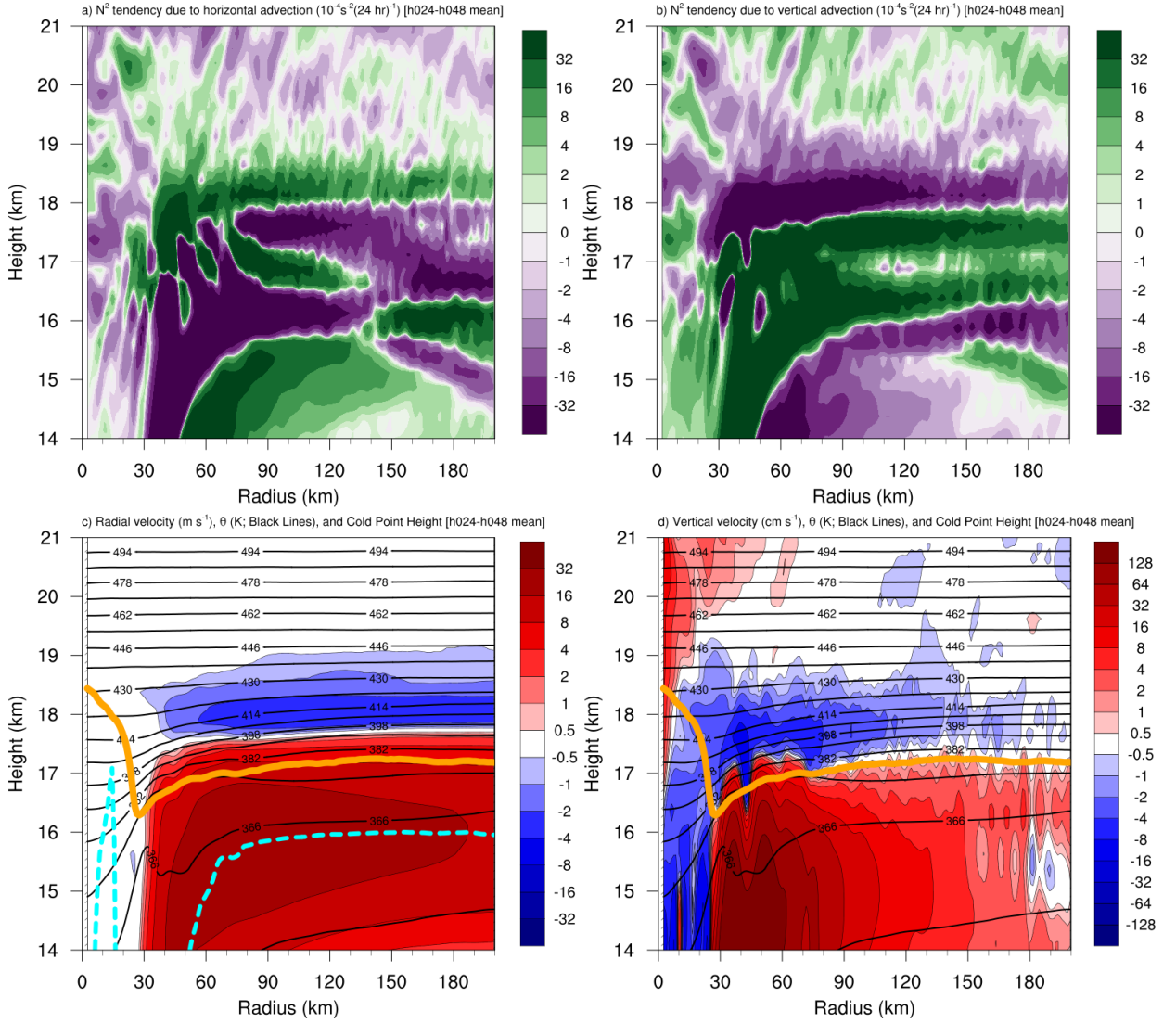


FIG. 8. The contribution to the change in N^2 over the 24-48-hour period ($10^{-4} \text{s}^{-2} (24 \text{ hr})^{-1}$) by (a) horizontal advection and (b) vertical advection. (c) The radial velocity (m s^{-1} ; filled contours), potential temperature (K; thick black contours), cold-point tropopause height (orange line), and level of maximum outflow (dashed cyan line) averaged over the 24-48-hour period. (d) The vertical velocity (cm s^{-1} ; filled contours), potential temperature (K; thick black contours), and cold-point tropopause height (orange line) averaged over the 24-48-hour period.

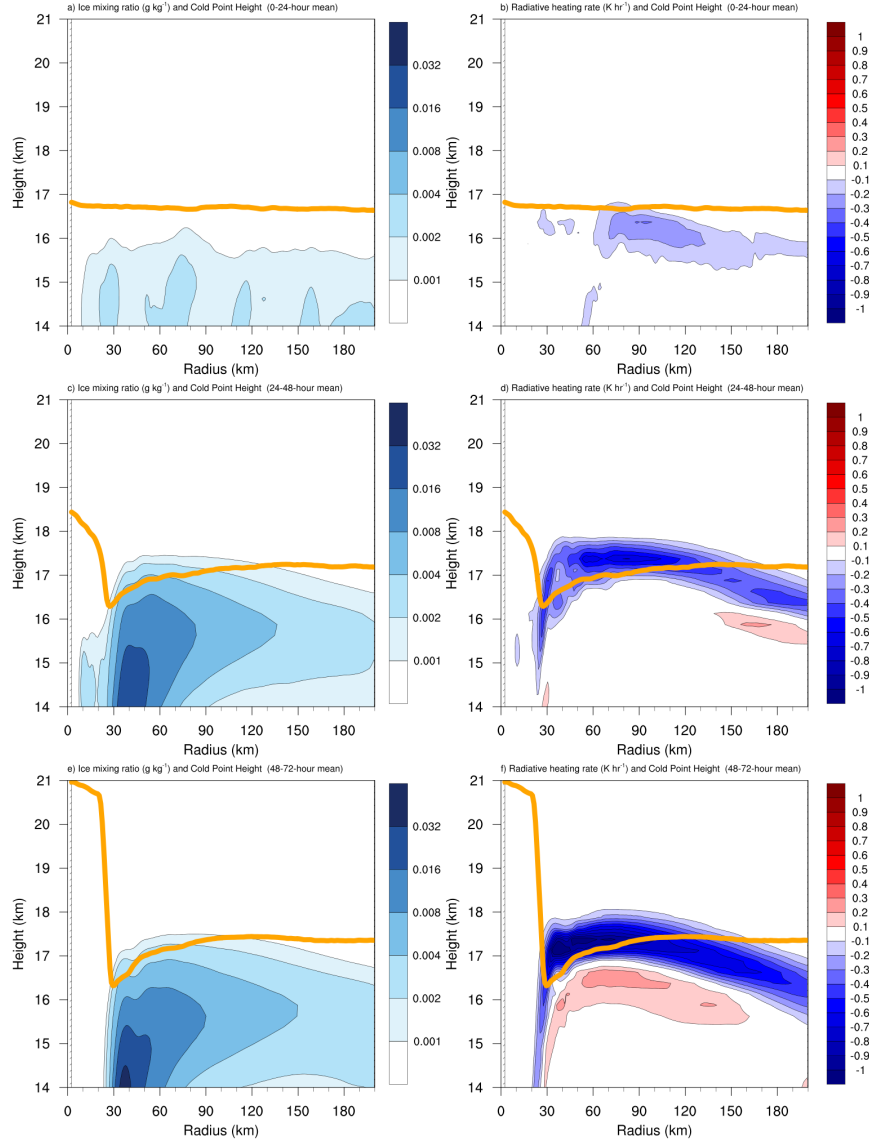


FIG. 9. Ice mixing ratio (g kg^{-1}) and cold-point tropopause height (orange lines) averaged over (a) 0-24 hours, (c) 24-48 hours, and (e) 48-72 hours. Radiative heating rate (K hr^{-1}) and cold-point tropopause height (orange lines) averaged over (b) 0-24 hours, (d) 24-48 hours, and (f) 48-72 hours.

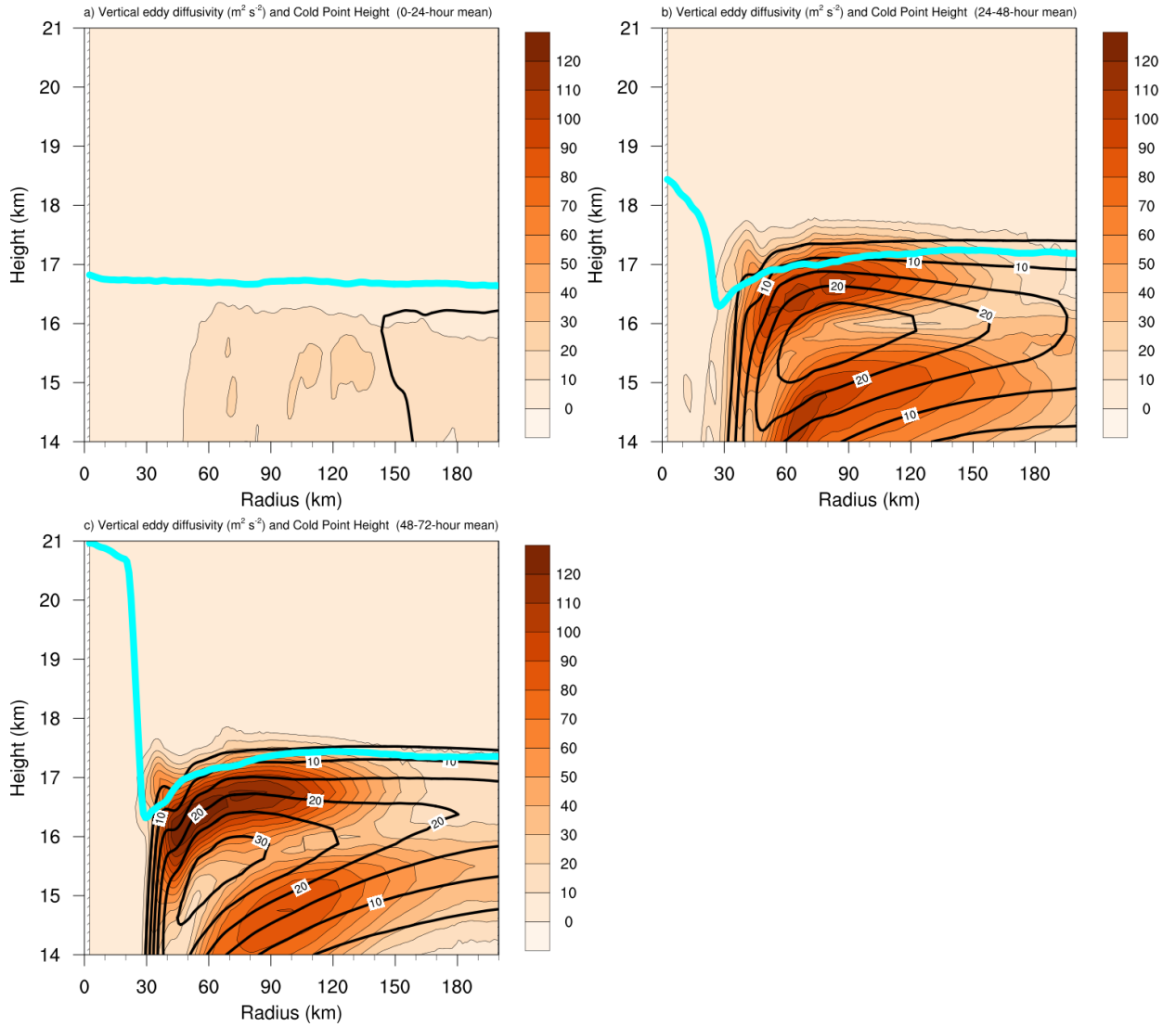


FIG. 10. Vertical eddy diffusivity ($\text{m}^2 \text{s}^{-2}$; filled contours), cold-point tropopause height (cyan lines), and radial velocity (m s^{-1} ; thick black lines) averaged over (a) 0-24 hours, (b) 24-48 hours, and (c) 48-72 hours.